

Effects of CO-dark Gas on Measurements of Molecular Cloud Stability and the Size-Linewidth Relationship

THEO J. O'NEILL,¹ RÉMY INDEBETOUW,^{1,2} ALBERTO D. BOLATTO,³ SUZANNE C. MADDEN,⁴ AND TONY WONG⁵

¹*Department of Astronomy, University of Virginia, Charlottesville, VA 22904, USA*

²*National Radio Astronomy Observatory, 520 Edgemont Road, Charlottesville, VA 22903, USA*

³*Department of Astronomy, University of Maryland, College Park, MD 20742, USA*

⁴*AIM, CEA, CNRS, Université Paris-Saclay, Université Paris Diderot, Sorbonne Paris Cité, 91191, Gif-sur-Yvette, France*

⁵*Department of Astronomy, University of Illinois, Urbana, IL 61801, USA*

ABSTRACT

Stars form within molecular clouds, so characterizing the physical states of molecular clouds is key in understanding the process of star formation. Cloud structure and stability is frequently assessed using metrics including the virial parameter and Larson (1981) scaling relationships between cloud radius, velocity dispersion, and surface density. Departures from the typical Galactic relationships between these quantities have been observed in low metallicity environments. The amount of H₂ gas in cloud envelopes without corresponding CO emission is expected to be high under these conditions; therefore, this “CO-dark” gas could plausibly be responsible for the observed variations in cloud properties. We derive simple corrections that can be applied to empirical clump properties (mass, radius, velocity dispersion, surface density, and virial parameter) to account for CO-dark gas in clumps following power-law and Plummer mass density profiles. We find that CO-dark gas is not likely to be the cause of departures from Larson’s relationships in low-metallicity regions, but that virial parameters may be systematically overestimated. We demonstrate that correcting for CO-dark gas is critical for accurately comparing the dynamical state and evolution of molecular clouds across diverse environments.

1. INTRODUCTION

Star formation is strongly correlated with tracers of molecular gas over kpc-scales (e.g., Kennicutt et al. 2007; Leroy et al. 2008; Bigiel et al. 2011), suggesting a causal relationship between the two. Since molecular clouds are the sites of star formation, understanding their dynamical states is necessary in accurately predicting star formation both in individual clouds as well as across larger populations.

Molecular hydrogen H₂ is the most abundant molecule in the interstellar medium (ISM) and is therefore closely tied to understanding the stability of molecular clouds and process of star formation. H₂ is a symmetric, homonuclear molecule with widely spaced rotational energy levels and no permanent dipole moment; as a consequence of this, it radiates very weakly and is difficult to observe directly under conditions typical of molecular clouds ($T \sim 10\text{--}20$ K). It is therefore necessary to use more accessible molecules as tracers of H₂ to fully understand the conditions under which stars form.

CO is one of the next most abundant molecules in the ISM and can be excited easily at low temperatures, making it a popular tracer of H₂. Using CO as a tracer, the amount and spatial distribution of molecular gas in a

region is often used to infer the process of star formation; however, this use of CO as a proxy for H₂ relies on the assumption that it faithfully traces the full spatial extent of H₂. It is well known that some portion of the H₂ in molecular clouds is not traced by CO: since CO is less efficient at shielding itself from FUV radiation than H₂ is, the transition from C⁺ to CO occurs closer to the center of clouds than the transition from H I to H₂, resulting in a central CO-traceable region surrounded by an extended diffuse envelope of “CO-dark” H₂.

Recent studies have simulated the formation of H₂ and CO in the ISM to evaluate the expected amount of CO-dark H₂ in a variety of environments (e.g. Glover et al. 2010; Glover & Mac Low 2011; Li et al. 2018; Gong et al. 2018). Wolfire et al. (2010, hereafter W10) modeled photodissociation regions (PDRs) of individual spherical clouds and defined the fraction of molecular H₂ mass not traced by CO, or “dark gas fraction,” as

$$f_{DG} = 1 - \frac{M(R_{CO})}{M(R_{H_2})}, \quad (1)$$

where $M(r)$ represents the mass contained within a radius r , R_{CO} is the radius of the CO-traceable material at which the optical depth, τ , equals 1 in the $J = 1\text{--}0$

transition, and R_{H_2} is the radius at which half of the hydrogen in the envelope surrounding the CO clump is molecular and half is atomic. This model is shown in Figure 1. Assuming standard Galactic conditions, W10 derived $f_{DG} \sim 0.3$, a result which they found to be relatively insensitive to cloud and environmental properties. Other studies both of individual cloud envelopes and at galactic scales have derived $f_{DG} \sim 0.4$, but observed a stronger dependence on environmental properties (e.g., Smith et al. 2014; Szűcs et al. 2016).

Similar values of f_{DG} have been found through observational work. In studies of individual Galactic clouds, f_{DG} has been found to be $\gtrsim 0.3$ (e.g., Grenier et al. 2005; Abdo et al. 2010; Velusamy et al. 2010; Lee et al. 2012; Langer et al. 2014; Xu et al. 2016), and on galactic scales CO-dark gas has been inferred to be 0.2–0.3x as massive as the total atomic mass of the Milky Way and 1.2–1.6x as massive as its total CO-traced molecular mass (Planck Collaboration et al. 2011; Paradis et al. 2012).

The amount of CO-dark gas is expected to increase in high-radiation environments, with the $C^+/C^0/CO$ transition shifting even further into the cloud to reach higher overall column densities. Similarly, the dark-gas fraction is expected to increase in low-metallicity (low- Z) environments, where decreasing dust-to-gas ratios combine with typically stronger radiation fields to increase the efficiency of CO destruction (Madden et al. 2006; Gordon et al. 2011; Madden et al. 2020). H_2 can additionally be photodissociated via Lyman-Werner band photons, but since it can be optically thick under some A_V conditions it is able to remain self-shielded while CO is photodissociated. These effects have been supported observationally in the metal-poor outskirts of the Galaxy and in the Large and Small Magellanic Clouds (LMC and SMC, respectively, with $Z \sim 1/2 Z_\odot$ and $Z \sim 1/5 Z_\odot$) where $f_{DG} \gtrsim 0.8$ (Pineda et al. 2013; Jameson et al. 2018; Chevance et al. 2020).

Although much work has gone into quantifying the cause and amount of CO-dark gas in a variety of environments, the practical impact of this gas on interpretations of metrics of clump stability and evolution has not been explored in as much depth. Assessing the gravitational stability of clouds as measured by the virial parameter α_{vir} (Bertoldi & McKee 1992) or if clouds conform to “Larson’s relationships” between cloud radius, velocity dispersion, and surface density (Larson 1981) is ubiquitous in both theoretical and observational studies. In low- Z environments, departures from the typical values and relationships between these quantities for CO clouds under Galactic conditions have been observed (e.g., Bolatto et al. 2008; Hughes et al. 2013; Rubele et al. 2015; Ochsendorf et al. 2017; Kalari et al. 2020). CO-dark

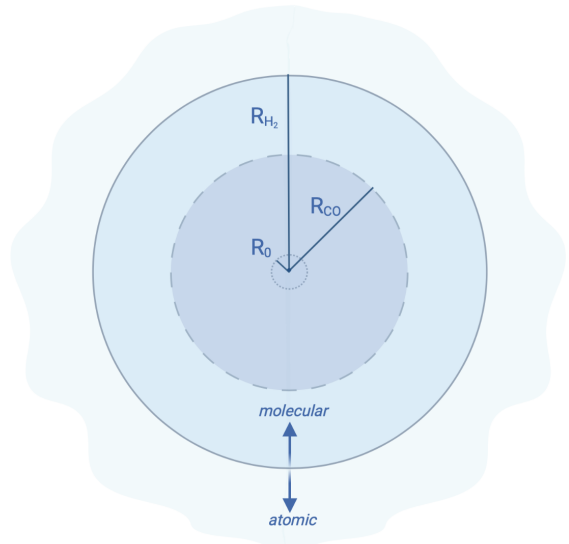


Figure 1. Clump toy model adapted from Wolfire et al. (2010). R_{H_2} is the radius at which the densities of atomic and molecular hydrogen are equal. Gas within R_{H_2} is mostly molecular and gas outside of R_{H_2} is mostly atomic. R_{CO} is the radius at which CO-traced material has $\tau = 1$ in the $J=1-0$ transition and is a function of f_{DG} , with higher f_{DG} yielding smaller R_{CO} . R_0 is the normalizing radius and is typically typically $\ll R_{CO}$. For a pure power-law density profile (§2.1) R_0 is arbitrary, while for a power-law profile with a core (§2.2) or Plummer profile (§2.3) it represents the radius of the flat central core.

gas could plausibly be responsible for these variations, since f_{DG} is known to be high in these regions and cloud properties inferred from CO-traced material are not guaranteed to be representative of the overall state of the structures. Correcting for CO-dark gas may then be an essential step in evaluating the dynamical states and likely futures of molecular clouds across a range of environments.

Here we present explicitly the variation in cloud properties from what would be inferred using CO-traceable material to the “true” state of clouds including CO-dark gas. In §2 we summarize mass density profiles that clouds may follow, derive corrections for empirical clump properties to account for CO-dark gas, and explore the behavior of α_{vir} as f_{DG} increases. We demonstrate the biases CO-dark gas creates in interpretations of size-linewidth-surface density scaling relationships in §3. We discuss the implications of our results and the effects of CO-dark gas on star formation in §4 before concluding in §5.

2. CLUMP DENSITY PROFILES

Analyzing the stability of molecular clouds ($R \gtrsim 10$ pc), clumps ($R \sim 1$ pc), and cores ($R \lesssim 0.1$ pc) is

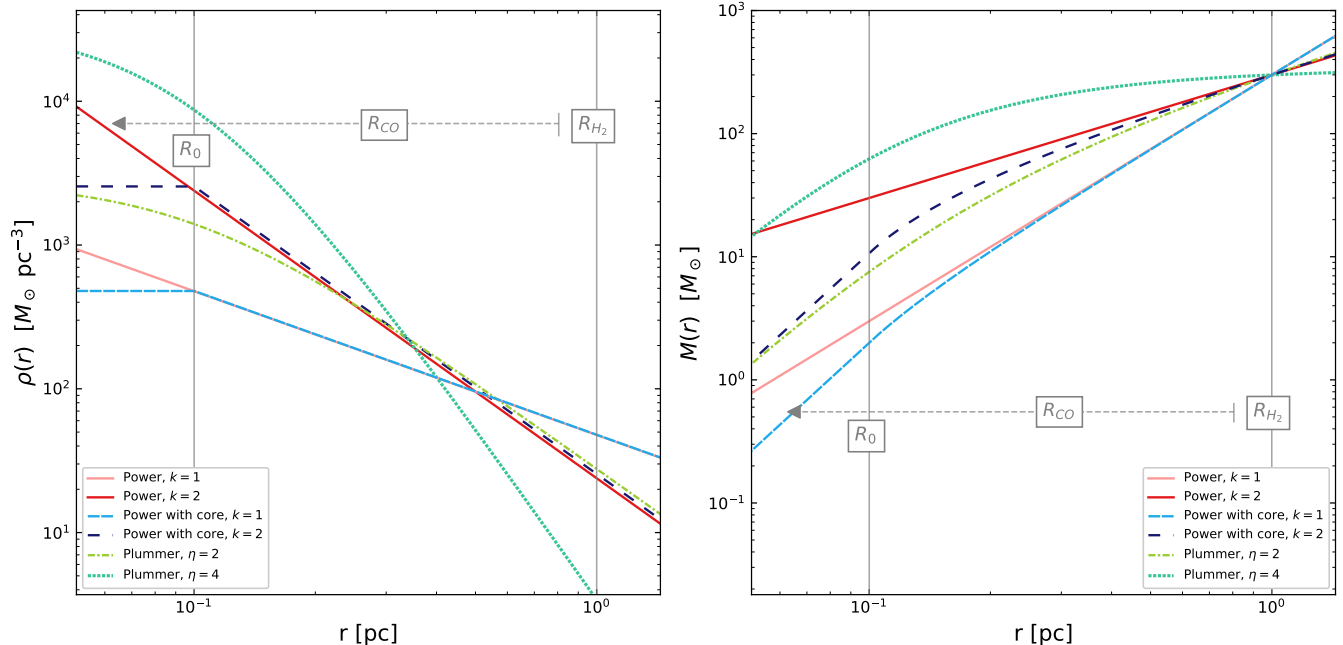


Figure 2. *Left:* Density as a function of radius for a clump with $[R_0 = 0.1 \text{ pc}, R_{H_2} = 1 \text{ pc}, M(R_{H_2}) = 300 M_\odot, \sigma_v(R_{H_2}) = 0.6 \text{ km s}^{-1}]$. R_0 and R_{H_2} are marked by the solid grey vertical lines, and the range of possible R_{CO} is shown by the dashed grey arrow. The solid pink and red curves are power-law profiles with $k = 1$ and $k = 2$, respectively (§2.1). The light blue densely-dashed and dark blue loosely-dashed curves are $k = 1$ and $k = 2$ power-laws with constant density cores, respectively (§2.2). The dash-dotted yellow-green and dotted light green curves are Plummer density profiles with $\eta = 2$ and $\eta = 4$, respectively (§2.3). *Right:* Total mass within r as a function of r for the fiducial clump, with the same line colors and styles as on the left.

of great interest to studies of their likely evolutionary futures. To this end, Bertoldi & McKee (1992) defined the virial parameter,

$$\alpha_{\text{vir}} = \frac{2\Omega_K}{|\Omega_G|} = \frac{M_{\text{vir}}}{M}, \quad (2)$$

as a measure of stability, where Ω_K is the kinetic energy, Ω_G is the gravitational potential energy, M is the structure’s mass, and M_{vir} is its virial mass. $\alpha_{\text{vir}} < 1$ suggests that the structure is gravitationally dominated and rapidly collapsing, $\alpha_{\text{vir}} \sim 1$ indicates that a structure is gravitationally stable, and $\alpha_{\text{vir}} \gg 1$ suggests that a structure is sub-critical and will likely expand unless confined by external pressure.

Variations from the expected equilibrium values of α_{vir} have been observed in environments where f_{DG} is known to be high. In Galactic environments, α_{vir} is frequently $\lesssim 2$ (see Kauffmann et al. 2013, for a review) in clumps and clouds. In nearby low- Z dwarf galaxies and low density, low-pressure environments, α_{vir} is frequently observed to be much larger and can reach measured values of 4–10 or more (e.g., Schrubba et al. 2017, 2019). Since these environments are rich in CO-dark gas, it is possible the measured α_{vir} could be unrepresentative of the states of full clumps, and that this additional molecular reservoir is responsible for the vari-

ations in measured α_{vir} . Alternatively, these differences could also be explained by measurement errors in σ_v and R stemming from large distance uncertainties, low velocity resolutions, or varying definitions of cloud radius.

For all clump density profiles that we will consider, we assume a one-dimensional radial velocity dispersion profile $\sigma_v(r)$ of

$$\sigma_v(r) = \left(\frac{r}{R_0}\right)^\beta \sigma_v(R_0), \quad (3)$$

where R_0 is a normalizing radius as shown in Figure 1. When considered in combination with a non-constant density profile $\rho(r)$, and if one considers turbulence to act as pressure support, our adopted Equation 3 leads to a gradient in energy density $\sim \rho\sigma_v^2$; we address the implications of this effect for cloud stability in §4. Additionally, we recognize that at very small scales (~ 0.1 pc) the effective pressure profile changes from thermal to non-thermal dominated support. Since the bulk of this work considers the effects of CO-dark gas on parsec-scales, this behavior should not impact our conclusions.

We analyze how the observationally-derived α_{vir} depends on observed CO radius for clouds following a single power-law (§2.1), a power-law with a constant density core (§2.2), and a Plummer profile (§2.3). We derive corrections for empirical clump properties at a given

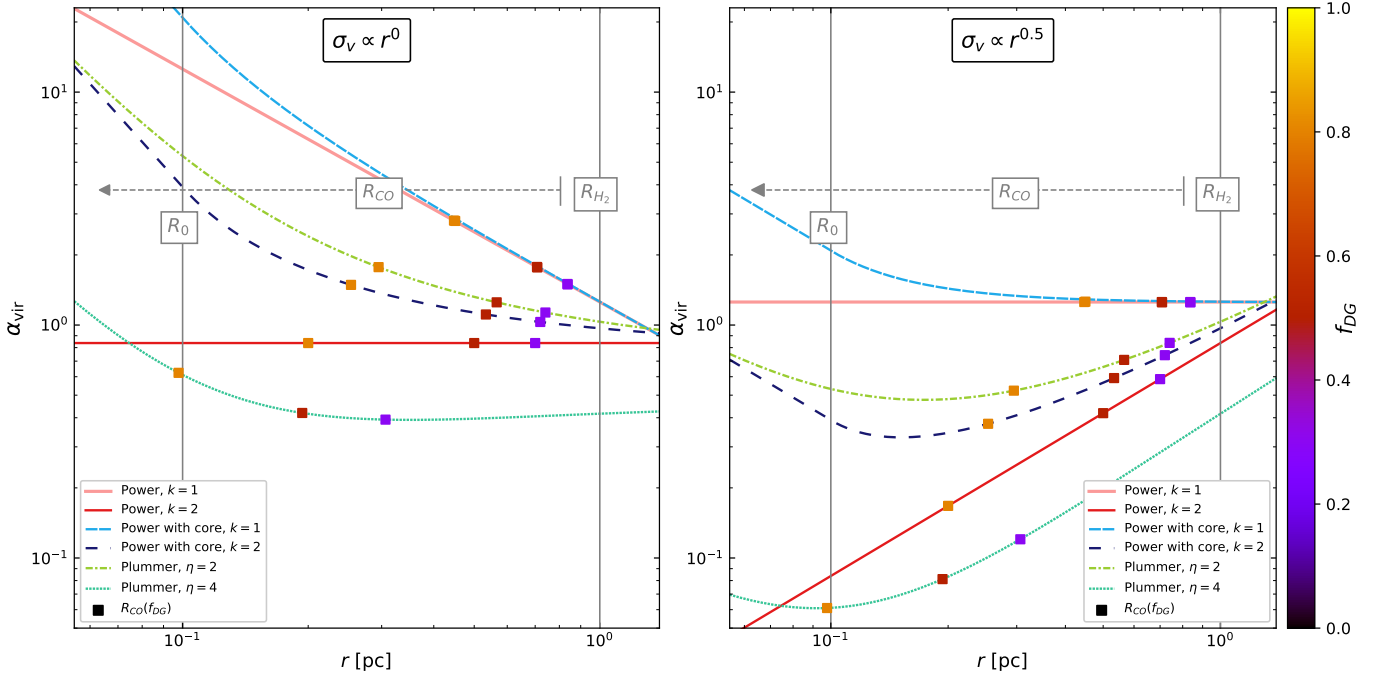


Figure 3. *Left:* The value of α_{vir} vs r for $\sigma_v \propto r^0$ [$\beta = 0$] for the clump shown in Figure 2 with [$R_0 = 0.1$ pc, $R_{H_2} = 1$ pc, $M(R_{H_2}) = 300 M_\odot$, $\sigma_v(R_{H_2}) = 0.6$ km s $^{-1}$]. The colors and styles of the profile curves, the R_0 and R_{H_2} lines, and the R_{CO} arrow are the same as in Figure 2. The square points along each curve mark the location of R_{CO} for that profile by value of f_{DG} . The purple points mark $f_{DG} = 0.3$, the red points mark $f_{DG} = 0.5$, and the orange points mark $f_{DG} = 0.8$. *Right:* Same as the left, but for $\sigma_v \propto r^{0.5}$ [$\beta = 0.5$].

dark-gas fraction f_{DG} . Finally, in §2.4 we compare the behaviors of the profiles considered and discuss the impact of density profile on the effects of CO-dark gas.

2.1. Power-law Profile

Clouds are very frequently modeled as having a density profile $\rho(r)$ following a simple power-law,

$$\rho(r) = \rho_c x^{-k}, \quad (4)$$

where ρ_c is the central density, $x = r/R_0$, and R_0 is an arbitrary radius at which ρ is normalized. Figure 2 shows $\rho(r)$ and mass $M(r)$ as a function of r for a clump with properties [$R_0 = 0.1$ pc, $R_{H_2} = 1$ pc, $M(R_{H_2}) = 300 M_\odot$, and $\sigma_v(R_{H_2}) = 0.6$ km s $^{-1}$] following $k = 1$ and $k = 2$.

In Appendix A.1, we derive the virial parameter for a clump following a power-law profile,

$$\alpha_{\text{vir}}(r) = \frac{3\sigma_v^2(r) T_1(r)}{\pi\rho_c G R_0^2 T_2(r)}, \quad (5)$$

where $T_1(r) = \left[\frac{4x^{(3-k)}}{(3-k)} \right]$ and $T_2(r) = \left[\frac{16x^{(5-2k)}}{(5-2k)(3-k)} \right]$. Figure 3 shows the variation of α_{vir} with r for the $k = 1$ and $k = 2$ profiles of the clump shown in Figure 2. We observe a large range of outcomes as r increases depending on the velocity and power-law indices adopted. For

[$k = 1$, $\beta = 0$], the cloud has decreasing α_{vir} value as radius increases; while for [$k = 1$, $\beta = 0.5$], α_{vir} is constant. Similarly for [$k = 2$, $\beta = 0$], α_{vir} is constant, and for [$k = 2$, $\beta = 0.5$], α_{vir} increases with radius.

We then cast these equations in terms of W10's f_{DG} for more insight and to derive corrections to observed molecular cloud properties for CO-dark gas. For a cloud following a power-law profile with $k < 3$, W10 defined

$$f_{DG} = 1 - \left(\frac{R_{CO}}{R_{H_2}} \right)^{3-k}. \quad (6)$$

We derive the variation in clump properties as a function of f_{DG} . Using the definition of f_{DG} in Equation 1, the total molecular mass within R_{H_2} can be found as

$$M(R_{H_2}) = \frac{M(R_{CO})}{1 - f_{DG}}. \quad (7)$$

From Equation 6 the relationship between R_{CO} and R_{H_2} is dependent on the adopted k ,

$$R_{H_2} = (1 - f_{DG})^{1/(k-3)} R_{CO}, \quad (8)$$

and with Equation 3 evaluated at $R_0 = R_{CO}$, $\sigma_v(R_{H_2})$ can be found as

$$\sigma_v(R_{H_2}) = (1 - f_{DG})^{\beta/(k-3)} \sigma_v(R_{CO}). \quad (9)$$

Using Equations 6 and 7, surface density $\Sigma(r) = M(r)/\pi r^2$ at R_{H_2} becomes

$$\Sigma(R_{H_2}) = (1 - f_{DG})^{(1-k)/(k-3)} \Sigma(R_{CO}). \quad (10)$$

The virial mass can be expressed in terms of f_{DG} as

$$M_{\text{vir}}(R_{H_2}) = (1 - f_{DG})^{(2\beta+1)/(k-3)} M_{\text{vir}}(R_{CO}). \quad (11)$$

Finally, the CO-dark-corrected virial parameter is

$$\alpha_{\text{vir}}(R_{H_2}) = \alpha_{\text{vir}}(R_{CO}) (1 - f_{DG})^{(2\beta+k-2)/(k-3)}. \quad (12)$$

In Figure 3 we show the values of R_{CO} and $\alpha_{\text{vir}}(R_{CO})$ as a function of f_{DG} for the fixed $R(H_2)=1$ pc clump: for $f_{DG} = 0.3$, $R_{CO} \simeq [0.85$ pc for $k = 1$, 0.7 pc for $k = 2]$, while for $f_{DG} = 0.5$, $R_{CO} \simeq [0.7$ pc for $k = 1$, 0.5 pc for $k = 2]$, and for $f_{DG} = 0.8$, $R_{CO} \simeq [0.45$ pc for $k = 1$, 0.2 pc for $k = 2]$.

We consider internal pressure for the power-law profile. Under a polytropic model, turbulent pressure within a cloud is described by $P \sim \rho \sigma_v^2$. By Equations 3 and 4, the pressure gradient for this profile then follows $dP/dx \sim (2\beta - k)x^{2\beta-k-1}$. Thus, if $2\beta - k < 0$ an outward pressure gradient conducive to stability will be present throughout the clump. Additionally, from Equation 12 we see that while $2\beta + k < 2$, $\alpha_{\text{vir}}(R_{H_2}) < \alpha_{\text{vir}}(R_{CO})$, i.e., the empirical α_{vir} from the CO-traced clump would overestimate the ‘‘true’’ α_{vir} of the full cloud including CO-dark gas. In this case, relying on the CO-derived measurement alone would lead to the incorrect conclusion that the cloud is dominated by kinetic energy, and either unbound or confined by high levels of external pressure.

2.2. Power-law Profile with a Constant Density Core

We also examine a cloud profile that follows a power-law at large r but has a small, constant density core of radius R_0 at its center,

$$\rho(r) = \begin{cases} \rho_c & \text{for } r < R_0 \\ \rho_c x^{-k} & \text{for } r \geq R_0, \end{cases} \quad (13)$$

where ρ_c is the central density and $x = r/R_0$. This has frequently been supported observationally, with $R_0 \lesssim 0.1$ pc (e.g., Girichidis et al. 2011; Juvela et al. 2018; Tang et al. 2018). We note that for this profile, unlike for the full power-law profile of §2.1, R_0 has a definite physical meaning, and that R_0 is typically $\ll R_{CO}$. In Figure 2, $\rho(r)$ and $M(r)$ are shown for $k = 1$ and $k = 2$ for a clump with an identical set of properties at R_{H_2} to the clump considered in §2.1 [$R_0 = 0.1$ pc, $R_{H_2} = 1$ pc, $M(R_{H_2}) = 300 M_\odot$, $\sigma_v(R_{H_2}) = 0.6$ km s $^{-1}$]. The

densities of this profile and of the full power-law profile described in §2.3 are roughly in agreement at about 0.5 pc; this is a consequence of the choice of R_0 and R_{H_2} , and changing their values changes this radius of agreement. In Appendix A.2, we follow the process outlined in §2.1 to derive the virial parameter for this profile,

$$\alpha_{\text{vir}}(r) = \begin{cases} \frac{15\sigma_v^2(r)}{4\pi\rho_c G R_0^2} \frac{1}{x^2} & \text{for } r < R_0 \\ \frac{3\sigma_v^2(r)}{\pi\rho_c G R_0^2} \frac{\Pi_1(r)}{\Pi_2(r)} & \text{for } r \geq R_0. \end{cases} \quad (14)$$

where $\Pi_1(r) = \left[\frac{4}{3-k} \left(x^{3-k} - \frac{k}{3} \right) \right]$ and

$$\Pi_2(r) = \begin{cases} \frac{16}{3-k} \left(\frac{x^{5-2k}-1}{5-2k} + \frac{k(1-x^{2-k})}{6-3k} + \frac{3-k}{15} \right) & \text{for } k \neq 2 \\ \frac{16}{3-k} \left(\frac{x^{5-2k}-1}{5-2k} - \frac{k \ln(x)}{3} + \frac{3-k}{15} \right) & \text{for } k = 2. \end{cases} \quad (15)$$

The variation of α_{vir} with r is shown in Figure 3 for $k = 1$ and $k = 2$. We observe a wide variety of behaviors as the area considered outside of the central core R_0 increases depending on the assumed density and velocity profiles. For both [$k=1$, $\beta=0$] and [$k = 2$, $\beta=0$], α_{vir} decreases rapidly with increasing x . For [$k = 1$, $\beta = 0.5$], α_{vir} plateaus marginally below the value of α_{vir} at $x = 1$, and for [$k = 2$, $\beta = 0.5$], it increases rapidly. Any conclusions as to whether the virial parameter of the CO-traceable material accurately represents the entire cloud, including CO-dark gas, are then extremely dependent on the assumptions made.

In Appendix A.2, we also derive

$$f_{DG} = \begin{cases} 1 - \left(\frac{3-k}{3} \frac{(R_{CO}/R_0)^3}{(R_{H_2}/R_0)^{(3-k)-\frac{k}{3}}} \right) & \text{for } R_{CO} < R_0 \\ 1 - \left(\frac{(R_{CO}/R_0)^{(3-k)-\frac{k}{3}}}{(R_{H_2}/R_0)^{(3-k)-\frac{k}{3}}} \right) & \text{for } R_{CO} \geq R_0, \end{cases} \quad (16)$$

assuming $R_{H_2} > R_0$. We show the value of R_{CO} as a function of f_{DG} in Figure 3 for $f_{DG} = 0.3, 0.5$, and 0.8. For $f_{DG} = 0.3$, $R_{CO} \simeq [0.85$ pc for $k = 1$, 0.7 pc for $k = 2]$, while for $f_{DG} = 0.5$, $R_{CO} \simeq [0.7$ pc for $k = 1$, 0.5 pc for $k = 2]$, and for $f_{DG} = 0.8$, $R_{CO} \simeq [0.45$ pc for $k = 1$, 0.25 pc for $k = 2]$.

We consider the limit of a clump with a very large central core, such that R_0 approaches R_{H_2} and k is effectively zero throughout the clump. In this case, we can derive a simplified kinetic term, $\Omega_k \propto x^{2\beta+3}$ and gravitational term $\Omega_G \propto x^5$, leading to

$$\alpha_{\text{vir}} \propto x^{2\beta-2}. \quad (17)$$

Therefore, while $\beta < 1$ the virial parameter will decrease as the radius r at which clump properties are evaluated increases. Most measurements of β on $\gtrsim 0.1$ pc scales

range between 0.2–0.5 (e.g., Heyer & Brunt 2004; Caselli & Myers 1995; Lin et al. 2021), so this condition appears easily met. We then expect that, if this condition were met, a full clump including CO-dark gas would have a lower α_{vir} than the result derived only from the CO-traced material, i.e., it would be more gravitationally dominated that could be inferred from CO alone.

2.3. Plummer Profile

The Plummer density profile (Plummer 1911) is frequently applied to molecular clouds and yields a small, flat inner core that transitions to a power-law profile at large radii. The Plummer profile follows

$$\rho(r) = \rho_c \left(\frac{1}{\sqrt{x^2 + 1}} \right)^\eta, \quad (18)$$

where ρ_c is the central density, R_0 is the radius of the central core, $x \equiv r/R_0$, and η is the index of the power-law at large radii. Pattle (2016) modeled the evolution of pressure-confined cores following Plummer-like density profiles in order to evaluate whether the cores were likely to collapse or to reach virial equilibrium as a function of radius. Here we extend this work in the context of CO-dark gas.

We derive corrections for CO-dark gas for two values of η : $\eta = 2$ as consistent with recent observational results ranging between $\eta = 1.5$ – 2.5 (e.g., Arzoumanian et al. 2011; Palmeirim et al. 2013; Zucker et al. 2021), and $\eta=4$ following Whitworth & Ward-Thompson (2001) and Pattle (2016). We adopt an internal cloud velocity dispersion profile following Equation 3. $\rho(r)$ and $M(r)$ are shown in Figure 2 for the fiducial clump with properties [$R_0 = 0.1$ pc, $R_{H_2} = 1$ pc, $M(R_{H_2}) = 300 M_\odot$, $\sigma_v(R_{H_2}) = 0.6$ km s $^{-1}$].

In Appendix A.3, we derive the virial parameter for this profile as

$$\alpha_{\text{vir}}(r) = \frac{3\sigma_v^2(r) P_1(r)}{\pi\rho_c GR_0^2 P_2(r)}. \quad (19)$$

where

$$P_1(r) = \begin{cases} 4(x - \arctan(x)) & \text{for } \eta = 2 \\ 2(\arctan(x) - \frac{x}{x^2+1}) & \text{for } \eta = 4, \end{cases} \quad (20)$$

and

$$P_2(r) = \begin{cases} 4P_1(r) - 16 \int_0^x \frac{x' \arctan(x')}{x'^2 + 1} dx' & \text{for } \eta = 2 \\ \arctan(x) + \frac{x-4 \arctan(x)}{x^2+1} + \frac{2x}{(x^2+1)^2} & \text{for } \eta = 4. \end{cases} \quad (21)$$

We similarly derive

$$f_{DG} = \begin{cases} 1 - \left(\frac{\frac{R_{CO}}{R_0} - \arctan(R_{CO}/R_0)}{\frac{R_{H_2}}{R_0} - \arctan(R_{H_2}/R_0)} \right) & \text{for } \eta = 2 \\ 1 - \left(\frac{\arctan(R_{CO}/R_0) - \frac{(R_{CO}/R_0)}{(R_{CO}/R_0)^2+1}}{\arctan(R_{H_2}/R_0) - \frac{(R_{H_2}/R_0)}{(R_{H_2}/R_0)^2+1}} \right) & \text{for } \eta = 4. \end{cases} \quad (22)$$

In Figure 3, we present the behavior of α_{vir} as a function of r for this profile. We also numerically solve for and plot the expected R_{CO} using Equation 22 for $f_{DG} = 0.3, 0.5,$ and 0.8 . For $f_{DG} = 0.3$, $R_{CO} \simeq [0.75$ pc for $\eta = 2, 0.3$ pc for $\eta = 4]$. For $f_{DG} = 0.5$, $R_{CO} \simeq [0.55$ pc for $\eta = 2, 0.2$ pc for $\eta = 4]$, and for $f_{DG} = 0.8$, $R_{CO} \simeq [0.3$ pc for $\eta = 2, 0.1$ pc for $\eta = 4]$.

As in the other profiles considered, the behavior of α_{vir} for the Plummer profile is highly variable and is dependent upon the density and velocity assumptions made. For a cloud with $\beta = 0$, α_{vir} is roughly constant for $x > 1$ and only marginally below the value of α_{vir} at $x = 1$. This indicates that the stability that would be inferred from just the CO-traced mass is a fairly accurate representation of the stability of the entire cloud. In contrast, for $\beta = 0.5$, α_{vir} increases rapidly above R_0 , suggesting that the CO-traced cloud would appear more gravitationally bound than the full cloud at R_{H_2} .

2.4. Comparison of Density Profiles

We consider the effect of the density profile on α_{vir} and the amount by which CO-dark gas changes observed clump properties. The impact of k/η on the overall value of α_{vir} is similar between all profiles considered, with smaller k leading to higher α_{vir} below R_{H_2} . In particular, α_{vir} is typically $\sim 2x$ larger for the power-law profiles of §2.1 and §2.2 than in the α_{vir} of the $\eta = 4$ Plummer profile. This is the result of the $\eta = 4$ Plummer profile having a much higher proportion of mass centrally concentrated at small r than the $k = 1$ and $k = 2$ power-law based profiles and $\eta = 2$ Plummer profile (see Figure 2).

Since $\Omega_G \sim GM^2/r$, concentrating a fixed amount of mass within a smaller area increases the object's gravitational potential and decreases the virial mass. In contrast, $\Omega_K \sim \sigma_v^2 M$ is not as dependent on the volume in which M is contained so it is unsurprising that α_{vir} is significantly reduced for the steeper profiles. Very sub-virial clumps are expected to rapidly collapse, and so to offset this effect and move closer to stability at R_{H_2} , the Plummer profile would need to have a much higher $\sigma_v(R_{H_2})$. The assumed radial velocity dispersion index β also has a large impact on clump dynamical state and the α_{vir} that would be inferred after correcting for CO-dark gas. For all profiles considered in this section, the

choice of β generally corresponds to the “direction” of the behavior of α_{vir} with r , whether increasing, decreasing, or constant.

Throughout this work, we use f_{DG} for a given clump as a set parameter, without attempting to tie its specific value to the underlying physics that determine the value of f_{DG} . In reality, f_{DG} is a function of the properties of the clump and the environment in which it is immersed. Since we aim to derive corrections that may be applied by observers using a specific assumed or measured value of f_{DG} to estimate clump properties, accounting for the nuances of the physical drivers of f_{DG} is beyond the scope of this work. However, we do expect that clumps with steeper density profiles will have lower f_{DG} than clumps with shallower profiles occupying the same environment under identical conditions.

We can intuitively consider that, in a given environment, a specific A_V /density threshold must be reached for CO to effectively self-shield (determined by radiation field strength, dust-to-gas ratio, etc). Since steeper profiles are more centrally concentrated in mass, they would contain a larger fraction of the total clump mass at this density floor where CO begins to be destroyed (R_{CO}); this would decrease f_{DG} despite being in an identical environment to a shallower clump.

Finally, we evaluate the overall effect of the internal density profile assumed on inferred CO-dark-corrected clump properties. For the fixed R_{H_2} we consider, the derived R_{CO} for a given f_{DG} decreases with increasing k (or η) because of our assumption that $R_0 \ll R_{CO}$. The values of R_{CO} and $\alpha_{\text{vir}}(R_{CO})$ for a power-law with core profile with $k = 1$ are functionally identical to those for a full power-law, and for a $k = 2$ power-law with core profile depart only slightly from the values derived from a full $k = 2$ power-law. Under most scenarios where $R_0 \ll R_{CO}$, the corrected properties (R_{H_2} , $\alpha_{\text{vir}}(R_{H_2})$, etc) derived for the power-law with core profile vary by a small amount (generally $\lesssim 10\%$ difference) from the corrections for a full power-law. The difference between corrected properties between profiles increases with increasing f_{DG} . The difference in corrected values between the steep $\eta = 4$ Plummer and power-law profiles is larger, but this is likely more of an effect of the variation in assumed η vs. k than of profile itself; the $\eta = 2$ profile also typically differs by $\lesssim 10\%$ from the power-law based profiles.

Therefore, we conclude that the relative steepness by which density decreases with r has a larger impact on the effects of CO-dark gas on observed clump properties than the exact form of the radial density profiles we consider. For the remainder of this work, we focus

our analysis on the behavior of clumps following single power-law profiles for simplicity.

3. CO-DARK GAS AND SIZE-LINEWIDTH-SURFACE DENSITY RELATIONSHIPS

3.1. Larson’s Scaling Relationships

Larson (1981) observed correlations between the size R , velocity dispersion σ_v , and mass surface density Σ of Galactic molecular clouds that have been confirmed and refined by later studies. The first of these relationships is a power-law relationship between the size of a cloud R and σ_v , where

$$\sigma_v \simeq C \left(\frac{R}{1 \text{ pc}} \right)^\Gamma \text{ km s}^{-1}. \quad (23)$$

Larson (1981) originally derived $\Gamma = 0.38$ and $C = 1.1 \text{ km s}^{-1}$, an estimate that Solomon et al. (1987) and Heyer et al. (2009) (hereafter SRBY and H09, respectively) later refined to

$$\sigma_v \simeq 0.72 \left(\frac{R}{1 \text{ pc}} \right)^{0.5} \text{ km s}^{-1}. \quad (24)$$

Larson’s second relationship is derived from observed correlations between σ_v and cloud mass M ,

$$\frac{2\sigma_v^2 R}{GM} \simeq 1, \quad (25)$$

which is usually interpreted as meaning that most clouds are roughly in virial equilibrium. Alternatively, it has been suggested that this is a signature of global hierarchical collapse at all scales within clouds (Ballesteros-Paredes et al. 2011; Vázquez-Semadeni et al. 2019). Finally, cloud density and size are observed to be inversely related, $n \propto R^{-1.1}$, suggesting that surface density is independent of size and should be roughly constant for clouds under conditions similar to the Milky Way, although observations have suggested that Σ does vary over several orders of magnitude with environment (e.g., H09; Sun et al. 2018; Traficante et al. 2018; Dessauges-Zavadsky et al. 2019; Chevance et al. 2020).

As noted by H09, a natural extension of these relationships is an association between surface density Σ and the size-linewidth parameter σ_v^2/R . A virialized sphere following a power-law density distribution should follow

$$\frac{\sigma_v^2}{R} = \frac{(3-k)}{3(5-2k)} \pi G \Sigma. \quad (26)$$

In Figures 4 and 5, we compare the relationships between R , σ_v , and Σ for structures observed using CO as a tracer across a variety of environments:

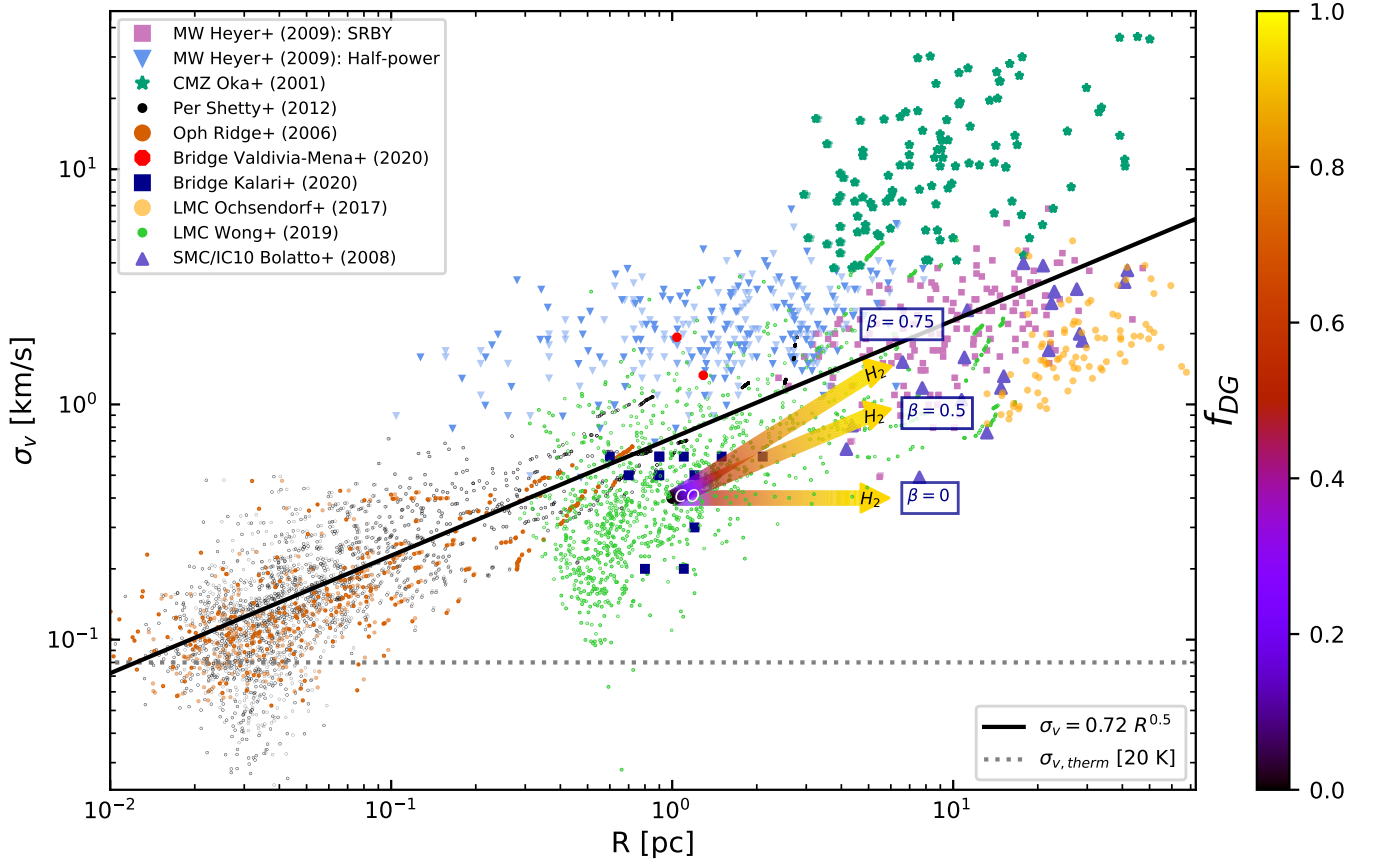


Figure 4. Velocity dispersion σ_v compared to radius R of CO-traced structures described in §3. The black line follows the relationship $\sigma_v = 0.72R^{0.5}$ (Equation 24) and the grey dotted line shows the expected contribution from thermal motion to σ_v at $T=20$ K. The arrows show the direction in which one would correct observed CO-traced clump properties for CO-dark gas to recover the properties of the full H_2 clump. The arrows start at physical properties typical of parsec-scale CO-traced clumps, and move towards the inferred properties of the H_2 clump. Each arrow is labeled with the power-law index k and velocity dispersion index β assumed to generate its path, and the color gradient along the arrows shows the corrected H_2 properties as a function of f_{DG} .

1. Galactic giant molecular clouds (GMCs), with sub-samples with areas defined from ^{12}CO by SRBY and from the ^{13}CO half-power contours of their central cores (H09);
2. clouds in the Galactic central molecular zone (Oka et al. 2001);
3. cores observed in the Ophiuchus molecular cloud (Ridge et al. 2006);
4. cores in the Perseus molecular cloud (Shetty et al. 2012);
5. Clumps in the Magellanic Bridge (Kalari et al. 2020; Valdivia-Mena et al. 2020);
6. Clumps in the LMC regions 30 Doradus, A439, GMC 104, GMC 1, PCC, and N59C (Wong et al. 2019);
7. GMCs in ~ 150 star-forming regions throughout the LMC (Ochsendorf et al. 2017);

8. Clouds in the SMC and dwarf galaxy IC 10 (Bolatto et al. 2008),

(where the choice of terminology core/clump/cloud corresponds to commonly used size scales of $\sim 0.1/1/10$ pc, without any differences in relevant physics implied).

In Figure 4 where R and σ_v are compared, the usual size-linewidth relationship of Equation 24 is displayed. Σ and σ_v^2/R are compared in Figure 5 for a subset of the sources listed above that have cloud mass estimates derived without assuming virial equilibrium (1, 6, 7, 8 in the list above). Equation 26 is shown as the straight black line for $k = 0$. Additionally, in pressure-bounded virial equilibrium, Σ and σ_v^2/R are related as (Field et al. 2011)

$$\frac{\sigma_v^2}{R} = \frac{1}{3} \left(\pi\gamma G\Sigma + \frac{4P_e}{\Sigma} \right), \quad (27)$$

which is shown in Figure 5 by the V-shaped curves, with $\gamma = 0.6$ for a cloud with $k = 0$.

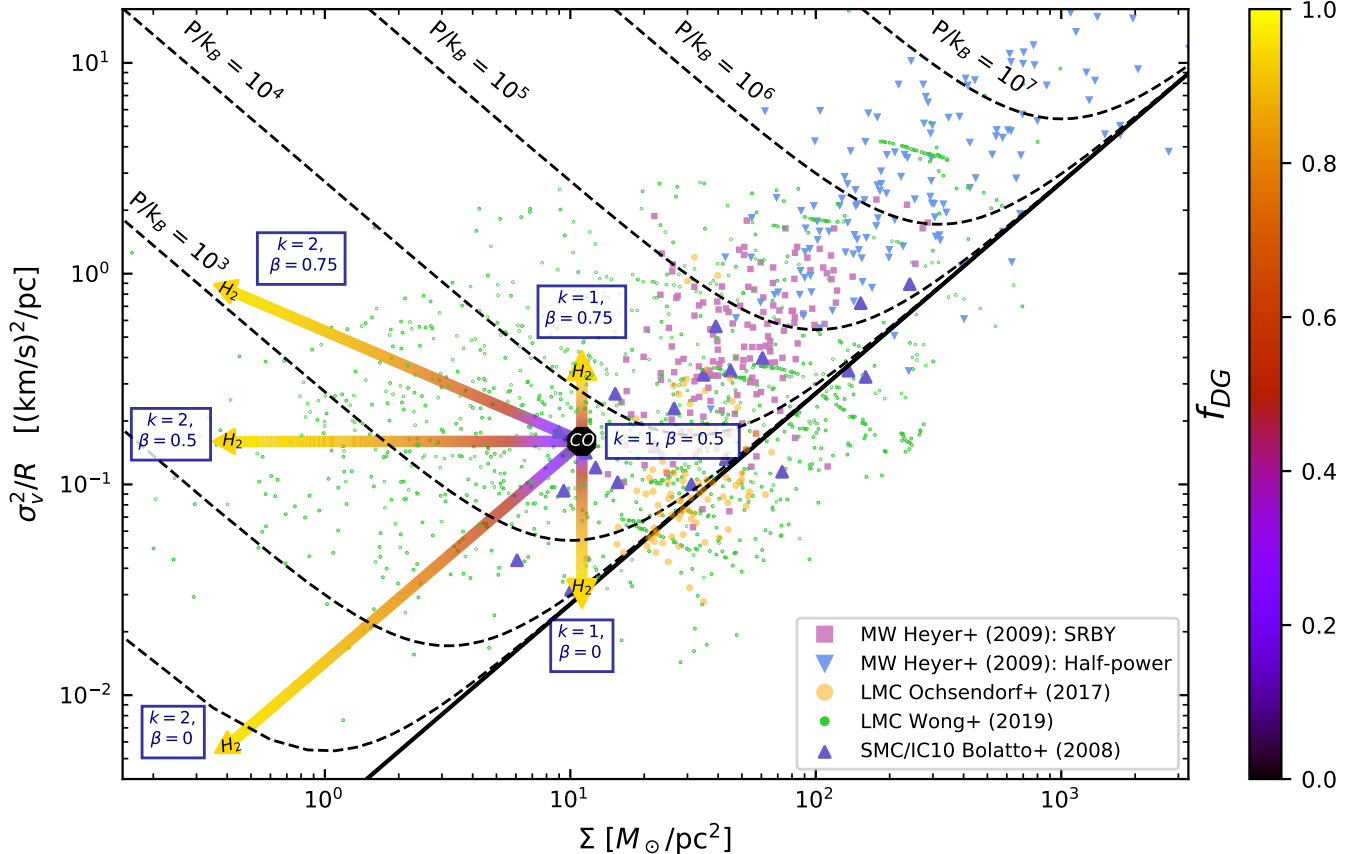


Figure 5. Size-linewidth parameter σ_v^2/R compared to surface density Σ for CO-traced structures described in §3. The black line corresponds to virial equilibrium without external pressure (Equation 26) and the dashed black curves correspond to virial equilibrium under external pressure with units for P/k_B labels in K cm^{-3} (Equation 27). The arrows are as in Figure 4 and show the direction in which one would correct observed CO-traced clump properties to recover the properties of the full clump including CO-dark H_2 .

The majority of the Wong et al. (2019) and Ochsendorf et al. (2017) LMC GMCs, Kalari et al. (2020) Bridge clumps, and Bolatto et al. (2008) SMC and IC 10 clouds have **smaller σ_v for a given R than expected from Galactic clouds**, falling well under the relationship described in Equation 24. This has been observed in a variety of other low- Z environments as well, e.g. by Rubio et al. (2015) in the $Z \simeq 0.13 Z_\odot$ dwarf galaxy Wolf–Lundmark–Melotte, and Hughes et al. (2013) in the LMC. Many of these samples also have lower Σ for a given σ_v^2/R than expected based on Equation 26, suggesting that the structures are either unbound and transient or must be confined by external pressure to remain stable, as position in this space is directly related to α_{vir} .

As part of the PHANGS-ALMA collaboration (“Physics at High Angular-resolution in Nearby Galaxies with ALMA,” Leroy et al. 2021), Sun et al. (2020) analyzed the dynamical states of molecular gas in 28 nearby disk galaxies. They derived typical midplane

pressures over 1 kpc scales ranging from $P/k_B = 10^3$ – 10^6 K cm^{-3} , and found that the average internal turbulent pressure of clouds was typically very similar to the required cloud-scale equilibrium pressure, which they concluded indicated that most gas was in dynamical equilibrium. Wong et al. (2009) derived an average midplane hydrostatic pressure in the central regions of the LMC of $P/k_B \sim 10^4 \text{ K cm}^{-3}$ using HI and $\text{CO}(1-0)$ observations, which could be sufficient to confine a large fraction of the Wong et al. (2019) LMC clumps observed to have high σ_v^2/R , as well as the majority of the Ochsendorf et al. (2017) LMC GMCs.

3.2. Effects of CO-dark Gas on Observed Relationships

The effects of our derived corrections for CO-dark gas in a power-law density profile clump (§2.1: Equations 8, 9, and 10) are shown by the arrows in Figures 4 and 5. The arrows start at the properties of a clump as observed solely in CO and move towards the “true” characteristics of the full clump including CO-dark gas, with color gradients along the arrow corresponding to f_{DG} . The initial

conditions for the corrections displayed are [$R_{CO} = 1$ pc, $\sigma_v(R_{CO}) = 0.4 \text{ km s}^{-1}$, $M(R_{CO}) = 35 M_{\odot}$]; these values correspond to the medians of these quantities for roughly pc-scale CO clumps in the Wong et al. (2019) sample. Changing the arrow’s origin does not impact the direction of the arrow. In Figure 4a, we only show corrections for $k = 1$, with arrows for $\beta = 0$, $\beta = 0.5$, and $\beta = 0.75$; this is because the corrections for $k = 1$ vs $k = 2$ overlap in this space and differ only in the extent to which their arrows extend. In Figure 5 we also show corrections for $k = 2$.

For $\beta = 0$, correcting for CO-dark gas causes clumps to have even lower σ_v relative to the increased R and thus drives the clumps further from following Equation 24. We note that a velocity profile this “flat” is unlikely, as turbulence within the ISM is mainly driven at large scales (Brunt et al. 2009), but we display it to demonstrate the limits of this effect. For $\beta = 0.5$, the corrections have no effect on the position of the clump in size-linewidth space relative to the expected Equation 24 relationship; this is because the standard inter-clump relationship Equation 24 and the displayed intra-clump profile share the same $\beta = \Gamma = 0.5$. By the same logic, $\beta = 0.75$ unsurprisingly brings clumps closer to agreement with Equation 24 because $\beta > \Gamma$. Corrections in Σ vs. σ_v^2/R space have a similarly variable effect. The distance of any given clump from the virial line in Figure 5 is directly proportional to the stability of the clump as measured by α_{vir} and we interpret the corrections for a power-law profile in this context as follows.

- We again see that the assumed k and β have a large impact on the inferred corrected state: for $k = 1$, Σ is constant; while for $k > 2$, the corrected Σ is significantly reduced.
- We observe that clumps decrease in α_{vir} and move towards $\alpha_{\text{vir}} \sim 1$ in all cases where $k + 2\beta < 2$. This suggests that, if these profile conditions are met, the apparently high α_{vir} structures traced by CO in low- Z , high f_{DG} environments may be closer to stability than expected.
- In most cases, the updated clump positions suggest that a lower level of external pressure would be required to maintain stability than would be inferred from CO-traced material alone.

The assumed density and velocity profiles then almost entirely determine the “direction” of these biases. This highlights the importance of studies of the spatial dependence of density and linewidth on the scale of individual clouds in addition to SRBY/H09-type studies comparing these quantities between cloud populations.

4. DISCUSSION

4.1. Can CO-dark Gas Explain Departures from Larson’s Relationships?

From the clump property corrections derived in §2 and described in §3, it is clear that neglecting CO-dark gas could significantly bias the assessment of cloud placement in Larson’s relationships and gravitational stability. We now examine if this effect is sufficient to explain the observed high α_{vir} and departures from Larson’s relationships in low- Z environments.

Under the corrections for a power-law profile that we have derived, low- σ_v clumps must follow an internal velocity profile with $\beta > 0.5$ (i.e., have large motions at large scales) to reconcile with the typical size-linewidth relationship described by Equation 24; however, large β s also yield increased α_{vir} that imply the full structure is gravitationally unbound. If instead one assumes that clouds are close to virialized without external pressure, then the dark gas correction required to move observed points closer to virialization (i.e., to decrease α_{vir}) requires that clumps follow a shallow density profile and have $\beta < 0.5$ — but, shallow β s increase the amount by which these clouds fall “under” the R - σ_v relationship of Equation 24.

This contradiction is most problematic in structures with high f_{DG} as expected in low- Z or high-radiation environments, and can be resolved if clouds in these areas are: (1) overwhelmingly gravitationally unstable and dispersing rapidly as a result; or (2) require much higher levels of external pressure to remain stable than clouds in more typical environments; or (3) possess a global σ_v/R trend shifted to lower values of σ_v than the classical Equation 24 relationship (i.e., a smaller scaling coefficient C in Equation. 23) and have shallow internal density and σ_v profiles ($0 \leq \beta < 0.5$).

(1) is unlikely statistically simply because of the number of clouds that are observed, and a physical cause for (2) is hard to imagine since the typical ISM pressure in low- Z galaxies is ~ 1 – 2 orders of magnitude smaller than in typical large spiral galaxies (de los Reyes & Kennicutt 2019). There are also nontrivial direct relationships between metallicity and ISM pressure in these areas because of reduced cooling and thermal balance, but predictions as a function of metallicity are generally only possible in the context of a self-regulated star formation model and thus the specifics depend on the details of that model. Additionally, the direct effects of metallicity via the cooling rate on pressure are less important than the galaxy type to the properties of molecular clouds

(3) is then the most compelling, and would be the simplest way to account for observed low- σ_v and high

α_{vir} structures in low- Z areas. Shallow density profiles of $1.5 < k < 2$ are typical on the pc-scales where the simplified isolated spherical PDR model that we consider here holds (Caselli et al. 2002; Pirogov 2009; Arzoumanian et al. 2011; Schneider et al. 2013), and even shallower profiles ($k \sim 1$) have been found in young, low-density cores and clumps (Chen et al. 2019, 2020; Lin et al. 2021). Small values of C and steep Γ relative to SRBY’s $C = 0.72$ and $\Gamma = 0.5$ have been derived from CO observations for structures in the SMC, LMC, and other local dwarf galaxies where low- σ_v / high α_{vir} structures are found (with $C \sim 0.2 - 0.6$ and $\Gamma \sim 0.55 - 0.85$) (Bolatto et al. 2008; Hughes et al. 2010, 2013; Wong et al. 2019). In CO-dark regions, HI can also be used as a probe of turbulence. For a sample of HI clouds in the LMC, Kim et al. (2007) derived a mean $\Gamma \simeq 0.5$.

In the pioneering Larson (1981) study, a shallow $\Gamma = 0.38$ was derived, which is similar to the Kolmogorov index for turbulent cascade in an incompressible medium $\beta \sim 1/3$. More recently, $\beta \simeq 1/2$ has frequently been found for GMCs both observationally and through simulations (e.g., Heyer & Brunt 2004; Dobbs 2015); this aligns the expectation for Burgers turbulence (Passot et al. 1988) i.e., in an isotropic system dominated by shocks, and is in accordance with SRBY’s $\Gamma = 0.5$. On very small scales ($\lesssim 0.05$ pc) a break in the internal size-linewidth relationship has been observed with β approaching zero (Goodman et al. 1998; Caselli et al. 2002; Volgenau et al. 2006; Pineda et al. 2010); however, it seems unlikely that the W10 scenario of PDRs of isolated individual spherical clouds surrounded by envelopes of dark gas would hold on these sizes because cores are typically embedded within larger structures.

Shallow values of β ($\beta \sim 0.2 - 0.3$) have also been derived in high mass star-forming regions (Caselli & Myers 1995) and in prestellar cores and young clumps (Tatematsu et al. 2004; Lee et al. 2015; Lin et al. 2021). Bertram et al. (2015) analyzed turbulence within simulated molecular clouds using the Δ -variance method, from which they compared the values of β within the full cloud, within H_2 gas, and within CO-traced material. For initial densities ranging between $30 - 100 \text{ cm}^{-3}$, the derived β ranged between $\sim 0.3 - 0.6$ as derived from the resulting H_2 density maps, and $\sim 0.15 - 0.4$ as traced by CO density, a difference which they attributed to the compact nature of the CO structures as compared to the more extended H_2 .

We emphasize that the inter-clump size-linewidth relationship with exponent Γ is obtained by comparing populations of clumps, while the intra-clump size-linewidth relationship with exponent β is obtained by studying individual structures. The latter relationship is much

more challenging to measure in the typically distant low- Z environments due to the required high angular resolutions and has only recently become possible, but is key for assessing if the implied shallow β is realistic. Overall, the measurements of β that have been obtained locally generally resemble observed values of Γ .

This observed correspondence of $\beta \sim \Gamma \simeq 0.5$ has been interpreted as reflecting the uniformity of velocity structure functions between individual clouds, so that Γ is largely set by β (Heyer & Brunt 2004). The implication from (3) that β is shallower than the observed Γ in low- Z environments creates some tension with this conclusion. One explanation for this difference could be a correlation between f_{DG} and cloud size. In their sample of LMC GMCs, Ochsendorf et al. (2017) observed a decrease in the ratio of CO-traced mass to dust-traced mass as dust-traced mass increased. Since the dust-traced mass likely includes the diffuse CO-dark gas, this suggests that a correlation between f_{DG} and cloud size exists with larger clouds having higher f_{DG} . Larger clouds would then systematically have larger relative changes between their true properties including CO-dark gas to their observed properties than smaller clouds do.

The “true” Γ relating the full clouds including CO-dark gas could then be shallower than the observed, CO-derived Γ , and instead approach (and possibly be determined by) the expected shallow β . This would explain the general steepness of CO-traced Γ in low- Z environments, as well as resolve the implied difference between β and Γ in low- Z environments. It is of course also possible that clumps in these low- Z environments do truly have different physical properties and scaling relationships than clumps under Galactic conditions.

4.2. CO-dark Gas and Star Formation

4.2.1. Star Formation Efficiency Considering CO-dark Gas

On kpc-scales, low- Z galaxies have been found to depart from the Kennicutt-Schmidt relationship, possessing higher star formation rate densities at a given molecular gas surface density as assessed by CO than found in more typical environments (e.g. Galametz et al. 2009; Schrubba et al. 2012). Star formation efficiency (SFE) is frequently assessed by comparing the star formation rate (SFR) to gas mass ($\epsilon' = \text{SFR} / M_{\text{cloud}}$), so this departure suggests that the SFE is also much higher than under Galactic conditions.

Madden et al. (2020) showed that CO-dark gas is sufficient to cause the apparent variation from the Kennicutt-Schmidt relationship on galactic scales, and that when corrected for the missing mass star formation in these environments is not significantly more efficient. It has also been suggested that H_2 gas is not a

requirement for star formation but is usually present as a consequence of the necessary shielding for stars to form (Glover & Clark 2012; Krumholz 2012). Star formation could then in principle proceed in atomic gas without the presence of molecular gas (although this would be rare), and may explain the lack of CO detections and corresponding high implied SFEs in some low-Z star-forming galaxies.

While CO-dark gas appears to be responsible for increased SFEs on large scales because surface densities averaged over large scales are increased by the addition of CO-dark gas mass, it is unclear how it impacts star formation in individual clumps. SFE is also frequently evaluated by simply comparing the total stellar mass to total molecular mass ($\epsilon = M_*/M_{\text{cloud}}$), or as a function of free-fall time ($\epsilon_{ff} = \tau_{ff} \times \epsilon'$). A simple but perhaps naive correction to the SFE of an individual CO-traced clump for missing H₂ mass would be $\epsilon_{H_2} = (1 - f_{DG})\epsilon_{CO}$ by Equation 7, with a similar correction for ϵ' . We have shown that CO-based observations are likely to overestimate mean clump density. This would lead to underestimates of free-fall time τ_{ff} and also, depending on density profile, potentially to underestimates of ϵ_{ff} as well.

However, the ϵ -based metrics are generally derived over larger scales, which helps offset the unknown variation from the original total gas mass for any given star-forming clump to its present day mass by averaging over clumps and cores at a variety of stages in the star formation process. Using the present-day gas mass of a single clump to try to derive a by-clump efficiency loses this advantage, and so we only suggest the use of the proposed corrected ϵ_{H_2} and related quantities on larger scales and even then with caution.

It is still not well understood if the actual way and timescale over which clouds collapse in low-Z environments is different than under conditions similar to the solar neighborhood, and, if so, how this departure influences the SFR/SFE. Parmentier (2020) and Parmentier & Pasquali (2020) derived a relationship between clump radial density profile and SFR and found that steeper profiles correspond to higher initial SFRs: star formation proceeds most rapidly in the densest areas of clumps, and the centers of clumps with very steep density profiles are denser than shallower clumps of the same mass.

Since radiation fields are known to be enhanced in the interclump medium due to the decreased dust-to-gas ratios, it is plausible that the typical radial profiles of clumps could be different than in higher-Z environments. We have shown that shallow density profiles are required for the properties of low-Z clumps to approximate those

of Galactic clumps, so it follows that in this scenario the low-Z clump-scale SFR could be slower than in higher-Z environments. To reconcile with the observed high SFR averaged over kpc-scales, relatively more clumps would need to exist to achieve these values.

Measurements of the total gas mass and SFR over large scales is clearly critical for these observations of SFE, and it is well understood that underestimating total mass can skew SFE estimates. An additional factor is the mechanics of how these clouds collapse to form stars at clump and core scales and the fraction of gas at these scales that actively contributes to star formation. The extent to which the diffuse CO-dark envelopes participate in star formation is unclear and is one of several contributing factors that sets SFE.

The scaling relationships between molecular gas and SFR observed over large scales can be validated by understanding the fraction of gas at clump-scales involved in star formation and the factors that affect the stability of individual cores and clumps. Detailed studies of the distribution and state of clumpy molecular gas is key in fully explaining the SFR/SFE and origin of scaling relationships at kpc-scales. Our models show the importance of CO-dark gas fraction and density and velocity dispersion profiles in influencing these properties. This work is then relevant to large scale measurements of SFEs in contextualizing interpretations of these measurements.

4.2.2. Relationship between f_{DG} and the CO-to-H₂ Conversion Factor

The corrections for CO-dark gas we have derived are dependent on having an estimate of the total molecular gas within R_{CO} , which could be derived through e.g., assuming local thermal equilibrium (LTE) with the use of multiple CO transitions, applying the non-LTE RADEX modeling, or similar methods. The widely-used CO-to-H₂ conversion factor

$$\begin{aligned} X_{CO} &= \frac{N(\text{H}_2)}{I_{CO}} [\text{cm}^{-2} (\text{K km s}^{-1})^{-1}] \\ \alpha_{CO} &= \frac{M_{\text{vir}}(R_{CO})}{L_{CO}} [M_{\odot} (\text{K km s}^{-1} \text{ pc}^2)^{-1}], \end{aligned} \quad (28)$$

is also designed to account for the untraced H₂ gas that we correct for in this work using f_{DG} . Some degree of correspondence between the two is then expected, as shown in previous works simulating the relationship between X_{CO} and environmental conditions (Shetty et al. 2011a,b; Clark & Glover 2015; Szűcs et al. 2016; Gong et al. 2018, 2020).

To demonstrate this expected relationship in the context of this work, we define a crude mass ratio factor

Y_{DG} where

$$Y_{DG} = \frac{M(R_{H_2})}{M(R_{CO})} = \frac{1}{1 - f_{DG}}, \quad (29)$$

by Equation 1. To compare the value of Y_{DG} across different environments, we define $Y_{DG,MW}$ as the typical value of Y_{DG} in the $f_{DG,MW}$ Milky Way. The expected Y_{DG} in a given environment can then be compared to $Y_{DG,MW}$ through the ratio of their respective f_{DG} ,

$$Y_{DG} = \left(\frac{1 - f_{DG,MW}}{1 - f_{DG}} \right) Y_{DG,MW}. \quad (30)$$

For a typical $Z \sim 1 Z_{\odot}$ Galactic environment with $f_{DG,MW} = 0.3$ (W10), $Y_{DG,MW} \simeq 1.4$. From this value, $Y_{DG} \simeq 3.5 Y_{DG,MW}$ would be expected in an environment like the $Z = 0.2 Z_{\odot}$ SMC with $f_{DG} \sim 0.8$ (Jameson et al. 2018). This corresponds very well to the observed ratio between the usual Galactic $X_{CO,MW}$ and X_{CO} derived in SMC clumps: for sub-pc clumps in the SMC Wing Muraoka et al. (2017) derived $X_{CO} \sim 4 X_{CO,MW}$, and for pc-scale clumps in the Magellanic Bridge Kalari et al. (2020) derived $X_{CO} \sim 3 X_{CO,MW}$ and Valdivia-Mena et al. (2020) found $X_{CO} \sim 1.5\text{--}3.5 X_{CO,MW}$. This suggests that Y_{DG} (and f_{DG}) could be used as a check of measured X_{CO} in clumps, or vice versa. In contrast, measurements of X_{CO} over cloud scales and larger ($\gtrsim 10$ pc) in the SMC have ranged between 20–50 $X_{CO,MW}$ (Leroy et al. 2009; Bolatto et al. 2011; Jameson et al. 2016), significantly exceeding the ratio between Y_{DG} and $Y_{DG,MW}$ that we have derived here.

This variation between X_{CO} and Y_{DG} estimates is likely caused by the well-known limits of X_{CO} at small scales (see Bolatto et al. 2013, for a review) and the limits of f_{DG} as formulated for isolated spherical PDRs by W10/in this work at large scales. When at low metallicities, X_{CO} is expected and observed to increase rapidly. On cloud and global scales, X_{CO} measurements are averaged over many clouds and so include both diffuse and dense molecular gas. For individual low- Z /high- f_{DG} clumps, though, only dense gas is reflected.

The scale (and resolution) at which clumps are measured is negatively associated with derived X_{CO} : in the LMC, for example, Fukui et al. (2008) derived $X_{CO} \sim 4 X_{CO,MW}$ from clouds observed at ~ 40 pc resolution by NANTEN, while Hughes et al. (2010) derived $X_{CO} \sim 2 X_{CO,MW}$ from structures observed at ~ 10 pc resolution by the Magellanic Mopra Assessment (MAGMA) survey. Lower-resolution observations run the risk of small clumps being diluted by large beam sizes, artificially inflating α_{vir} and X_{CO} and also increasing the likelihood of such clumps not being identified at all. Resolved observations of individual pc-scale

clumps in distant low- Z environments have only recently become possible and typically yield smaller conversion factors (Muraoka et al. 2017; Schruba et al. 2017; Saldaña et al. 2018; Kalari et al. 2020; Valdivia-Mena et al. 2020), approaching $X_{CO,MW}$ and in alignment with our expectations for clump f_{DG} .

4.3. Guidance for Interpreting Observations

We present the case of a “typical” observed CO clump with high α_{vir} , and discuss the properties that would be inferred by an observer using our derived corrections for CO-dark gas. For a clump following a typical $k = 1.5$ and $\beta = 0.5$ with [$R_{CO} = 1$ pc, $\sigma_v(R_{CO}) = 0.4$ km s^{-1} , $M(R_{CO}) = 35 M_{\odot}$, $\alpha_{vir}(R_{CO}) = 4.3$], a moderate Galactic $f_{DG} \sim 0.3$ (W10) yields a relatively small difference in clump properties: [$R_{H_2} = 1.3$ pc, $\sigma_v(R_{H_2}) = 0.45$ km s^{-1} , $M(R_{H_2}) = 50 M_{\odot}$, $\alpha_{vir}(R_{H_2}) = 4.8$]. In contrast, an extreme $f_{DG} \sim 0.9$ as occasionally derived in low- Z environments (Jameson et al. 2018) would lead to a significantly different set of inferred properties: [$R_{H_2} = 4.6$ pc, $\sigma_v(R_{H_2}) = 0.86$ km s^{-1} , $M(R_{H_2}) = 350 M_{\odot}$, $\alpha_{vir}(R_{H_2}) = 9.2$].

We then see that under typical assumed clump density and velocity profiles, correcting for CO-dark gas does *not* resolve the apparent instability of the structure — it actually exacerbates the issue. We emphasize again that the changes in clump properties post-correction are highly dependent upon the choice of k and β ; if the same clump followed shallower profiles, a reduction in α_{vir} could just as easily be indicated. At the same time, the magnitude of this shift makes clear that correcting for CO-dark gas is essential for an accurate assessment of clump properties in high f_{DG} environments.

5. CONCLUSIONS

We have derived easily-applied corrections to CO-derived clump properties to account for the effects of CO-dark gas. Our main conclusions are as follows:

1. For molecular clouds following power-law or Plummer density profiles, CO-derived measurements will systematically underestimate cloud mass and size. If clumps have shallow mass density and radial velocity dispersion profiles, the virial parameter α_{vir} will be overestimated (§2).
2. In order to interpret CO observations as accurately as possible, cloud properties (e.g., size, mass, surface density, velocity dispersion, virial parameter) should be corrected using the prescriptions outlined in §2 as demonstrated in §4.3.
3. CO-derived measurements are most suspect in low- Z , high f_{DG} regions; however, CO-dark gas

is unlikely to simultaneously be the cause of observed clumps with high α_{vir} and low σ_v relative to Larson's relationships in low-Z environments (§3, §4.1).

Understanding what other processes might drive departures from Larson's relationships and from inferred virial equilibrium should be of high priority. Attempts to correct for all of the above effects are reliant on accurate assessment of intra-cloud density and velocity profiles, and so this too should continue to be prioritized, especially on clump scales.

It is clear that assessing how star formation proceeds within clumps in low-Z regions is dependent on understanding the impact of CO-dark gas. Accounting for CO-dark gas both on local and global scales is then key in evaluating the evolutionary history and likely future of specific regions and in placing star formation in low-Z environments into its correct context. The corrections we have presented here are one tool to better leverage

CO observations to estimate clump behavior after accounting for the effects of environment.

1 We thank Kelsey Johnson, Allison Costa, and Molly
 2 Finn for useful comments and discussion. T.J.O. and
 3 R.I. were supported during this work by NSF award
 4 2009624. The National Radio Astronomy Observa-
 5 tory is a facility of the National Science Foundation
 6 operated under cooperative agreement by Associated
 7 Universities, Inc. This paper makes use of the follow-
 8 ing ALMA data: ADS/JAO.ALMA#2012.1.00683.S,
 9 ADS/JAO.ALMA#2015.1.1013.S, ADS/JAO.ALMA
 10 #2016.1.00193.S. ALMA is a partnership of ESO (rep-
 11 resenting its member states), NSF (USA) and NINS
 12 (Japan), together with NRC (Canada), MOST and
 13 ASIAA (Taiwan), and KASI (Republic of Korea), in
 14 cooperation with the Republic of Chile. The Joint
 15 ALMA Observatory is operated by ESO, AUI/NRAO
 16 and NAOJ.

Software: Astropy (Astropy Collaboration et al. 2013, 2018); BioRender (<https://biorender.com>); Matplotlib (Hunter 2007); Numpy (Harris et al. 2020)

APPENDIX

A. DERIVATION OF CLUMP DENSITY PROFILES

For a clump following a given density profile $\rho(r)$, the relevant terms for calculating the virial parameter and corrections for CO-dark gas that we derive are as follows. Mass within a radius r can be found as

$$M(r) = 4\pi \int_0^r r'^2 \rho(r') dr'. \quad (\text{A1})$$

This leads to gravitational potential energy

$$\Omega_G(r) = -4\pi G \int_0^r r' \rho(r') M(r') dr', \quad (\text{A2})$$

where G is the fundamental gravitational constant. We assume a one-dimensional radial velocity dispersion profile $\sigma_v(r)$ following Equation 3. The total kinetic energy can be found as

$$\Omega_K(r) = \frac{3}{2} M(r) \sigma_v^2(r), \quad (\text{A3})$$

and the virial mass $M_{\text{vir}}(r)$ follows from requiring $2\Omega_K(r) = -\Omega_G(r)$.

A.1. Power-law Profile

We consider a clump following a power-law profile,

$$\rho(r) = \rho_c x^{-k}, \quad (\text{A4})$$

where ρ_c is the central density, $x = r/R_0$, and R_0 is an arbitrary radius at which ρ is normalized. From Equation A1, the mass of such a structure is

$$M(r) = \pi \rho_c R_0^3 T_1(r), \quad (\text{A5})$$

where $T_1(r) = \left[\frac{4x^{(3-k)}}{(3-k)} \right]$. From Equation A2, the gravitational term is

$$\Omega_G(r) = -\pi^2 \rho_c^2 G R_0^5 T_2(r) = -\frac{GM(r)^2}{R_0} \frac{T_2(r)}{T_1(r)^2}, \quad (\text{A6})$$

where $T_2(r) = \left[\frac{16x^{(5-2k)}}{(5-2k)(3-k)} \right]$. (The use of $T_1(r)$ and $T_2(r)$ in these expressions will make the parallels with subsequent radial density profiles clearer.) From Equation A3, the kinetic term is

$$\Omega_K(r) = \frac{3}{2} \pi \rho_c R_0^3 T_1(r) \sigma_v^2(r). \quad (\text{A7})$$

Requiring $2\Omega_K = -\Omega_G$, we derive the virial mass

$$M_{\text{vir}}(r) = \frac{3\sigma_v^2(r)R_0}{G} \frac{T_1(r)^2}{T_2(r)}, \quad (\text{A8})$$

which is equivalent to the classical virial mass definition (Solomon et al. 1987; MacLaren et al. 1988)

$$M_{\text{vir}}(r) = \frac{3(5-2k)}{(3-k)} \frac{r \sigma_v^2(r)}{G}. \quad (\text{A9})$$

From Equation 2, the virial parameter is then

$$\alpha_{\text{vir}}(r) = \frac{3\sigma_v^2(r)}{\pi \rho_c G R_0^2} \frac{T_1(r)}{T_2(r)}, \quad (\text{A10})$$

which is equivalent to

$$\alpha_{\text{vir}}(r) = \frac{3(5-2k)}{4\pi \rho_c} \frac{\sigma_v^2(R_0)}{G} x^{2\beta+k-2}, \quad (\text{A11})$$

under the scaling of the velocity dispersion profile of Equation 3.

In their Appendix A, W10 derived the dark-gas fraction for a power-law density profile with $k < 3$ as

$$f_{DG} = 1 - \left(\frac{R_{CO}}{R_{H_2}} \right)^{3-k}. \quad (\text{A12})$$

R_{H_2} can then be solved for analytically, with $\Sigma(R_{H_2})$, $\alpha_{\text{vir}}(R_{H_2})$, and related properties following as demonstrated in §2.1.

A.2. Power-law Profile with Constant Density Core

We consider a clump following a power-law density profile with a uniform core of radius R_0 ,

$$\rho(r) = \begin{cases} \rho_c & \text{for } r < R_0 \\ \rho_c x^{-k} & \text{for } r \geq R_0, \end{cases} \quad (\text{A13})$$

where ρ_c is the central density and $x = r/R_0$. From Equation A1, the mass within r is

$$M(r) = \begin{cases} \pi \rho_c R_0^3 \left[\frac{4}{3} x^3 \right] & \text{for } r < R_0 \\ \pi \rho_c R_0^3 \Pi_1(r) & \text{for } r \geq R_0, \end{cases} \quad (\text{A14})$$

where $\Pi_1(r) = \left[\frac{4}{3-k} \left(x^{3-k} - \frac{k}{3} \right) \right]$. From Equation A2, the gravitational term is

$$\Omega_G(r) \equiv \begin{cases} -\frac{16}{15}\pi^2 G \rho_c^2 R_0^5 x^5 & \text{for } r < R_0 \\ -\pi^2 G \rho_c^2 R_0^5 \Pi_2(r) & \text{for } r \geq R_0, \end{cases} \quad (\text{A15})$$

where

$$\Pi_2(r) = \begin{cases} \frac{16}{3-k} \left(\frac{x^{5-2k}-1}{5-2k} + \frac{k(1-x^{2-k})}{6-3k} + \frac{3-k}{15} \right) & \text{for } k \neq 2 \\ \frac{16}{3-k} \left(\frac{x^{5-2k}-1}{5-2k} - \frac{k \ln(x)}{3} + \frac{3-k}{15} \right) & \text{for } k = 2. \end{cases} \quad (\text{A16})$$

From Equation A3, the kinetic term is

$$\Omega_K(r) = \begin{cases} 2\pi\rho_c R_0^3 x^3 \sigma_v^2(r) & \text{for } r < R_0 \\ \frac{3}{2}\pi\rho_c R_0^3 \Pi_1(r) \sigma_v^2(r) & \text{for } r \geq R_0. \end{cases} \quad (\text{A17})$$

Requiring $2\Omega_K = -\Omega_G$, we then define the virial mass

$$M_{\text{vir}}(r) = \begin{cases} \frac{5R_0\sigma_v^2(r)}{G} x & \text{for } r < R_0 \\ \frac{3R_0\sigma_v^2(r)}{G} \frac{\Pi_1(r)^2}{\Pi_2(r)} & \text{for } r \geq R_0, \end{cases} \quad (\text{A18})$$

and finally the virial parameter as

$$\alpha_{\text{vir}}(r) = \begin{cases} \frac{15\sigma_v^2(r)}{4\pi\rho_c G R_0^2} \frac{1}{x^2} & \text{for } r < R_0 \\ \frac{3\sigma_v^2(r)}{\pi\rho_c G R_0^2} \frac{\Pi_1(r)}{\Pi_2(r)} & \text{for } r \geq R_0. \end{cases} \quad (\text{A19})$$

We cast this profile in terms of f_{DG} as defined in Equation 1, such that

$$f_{DG} = \begin{cases} 1 - \left(\frac{3-k}{3} \frac{(R_{CO}/R_0)^3}{(R_{H_2}/R_0)^{(3-k) - \frac{k}{3}}} \right) & \text{for } R_{CO} < R_0 \\ 1 - \left(\frac{(R_{CO}/R_0)^{(3-k) - \frac{k}{3}}}{(R_{H_2}/R_0)^{(3-k) - \frac{k}{3}}} \right) & \text{for } R_{CO} \geq R_0, \end{cases} \quad (\text{A20})$$

assuming $R_{H_2} > R_0$. R_{H_2} can then be solved for analytically, with $\Sigma(R_{H_2})$, $\alpha_{\text{vir}}(R_{H_2})$, and related properties following.

A.3. Plummer Density Profile

We consider a clump following a Plummer density profile,

$$\rho(r) = \rho_c \left(\frac{1}{\sqrt{x^2 + 1}} \right)^\eta, \quad (\text{A21})$$

where ρ_c is the central density, $x = r/R_0$, R_0 is the radius of the central core, and η is the index of the power-law at large radii. From Equation A1, the mass within r is

$$M(r) = \pi\rho_c R_0^3 P_1(r), \quad (\text{A22})$$

where

$$P_1(r) = \begin{cases} 4(x - \arctan(x)) & \text{for } \eta = 2 \\ 2(\arctan(x) - \frac{x}{x^2+1}) & \text{for } \eta = 4. \end{cases} \quad (\text{A23})$$

From Equation A2, the gravitational term can be written as

$$\Omega_G(r) = -\pi^2 G \rho_c^2 R_0^5 P_2(r) = -\frac{GM(r)^2}{R_0} \frac{P_2(r)}{P_1(r)^2}, \quad (\text{A24})$$

where

$$P_2(r) = \begin{cases} 16 \left(x - \arctan(x) - \int_0^x \frac{x' \arctan(x')}{x'^2 + 1} dx' \right) & \text{for } \eta = 2 \\ \arctan(x) + \frac{x-4 \arctan(x)}{x^2+1} + \frac{2x}{(x^2+1)^2} & \text{for } \eta = 4. \end{cases} \quad (\text{A25})$$

From Equation A3, the kinetic term is

$$\Omega_K(r) = \frac{3}{2} \pi \rho_c R_0^3 \sigma_v^2(r) P_1(r). \quad (\text{A26})$$

We can then derive the virial mass through requiring $2\Omega_K = -\Omega_G$,

$$M_{\text{vir}}(r) = \frac{3R_0 \sigma_v^2(r) P_1(r)^2}{G P_2(r)}, \quad (\text{A27})$$

and finally the virial parameter

$$\alpha_{\text{vir}}(r) = \frac{3\sigma_v^2(r) P_1(r)}{\pi \rho_c G R_0^2 P_2(r)}. \quad (\text{A28})$$

We adapt this profile into f_{DG} as defined in Equation 1, such that

$$f_{DG} = \begin{cases} 1 - \left(\frac{\frac{R_{CO}}{R_0} - \arctan(R_{CO}/R_0)}{\frac{R_{H_2}}{R_0} - \arctan(R_{H_2}/R_0)} \right) & \text{for } \eta = 2 \\ 1 - \left(\frac{\arctan(R_{CO}/R_0) - \frac{(R_{CO}/R_0)}{(R_{CO}/R_0)^2+1}}{\arctan(R_{H_2}/R_0) - \frac{(R_{H_2}/R_0)}{(R_{H_2}/R_0)^2+1}} \right) & \text{for } \eta = 4. \end{cases} \quad (\text{A29})$$

R_{H_2} can then be solved for numerically to obtain estimates of $\Sigma(R_{H_2})$, $\alpha_{\text{vir}}(R_{H_2})$, and related properties.

REFERENCES

- Abdo, A. A., Ackermann, M., Ajello, M., et al. 2010, [ApJ](#), **710**, 133
- Arzoumanian, D., André, P., Didelon, P., et al. 2011, [A&A](#), **529**, L6
- Astropy Collaboration, Robitaille, T. P., Tollerud, E. J., et al. 2013, [A&A](#), **558**, A33
- Astropy Collaboration, Price-Whelan, A. M., Sipőcz, B. M., et al. 2018, [AJ](#), **156**, 123
- Ballesteros-Paredes, J., Hartmann, L. W., Vázquez-Semadeni, E., Heitsch, F., & Zamora-Avilés, M. A. 2011, [MNRAS](#), **411**, 65
- Bertoldi, F., & McKee, C. F. 1992, [ApJ](#), **395**, 140
- Bertram, E., Klessen, R. S., & Glover, S. C. O. 2015, [MNRAS](#), **451**, 196
- Bigieli, F., Leroy, A. K., Walter, F., et al. 2011, [ApJL](#), **730**, L13
- Bolatto, A. D., Leroy, A. K., Rosolowsky, E., Walter, F., & Blitz, L. 2008, [ApJ](#), **686**, 948
- Bolatto, A. D., Wolfire, M., & Leroy, A. K. 2013, [ARA&A](#), **51**, 207
- Bolatto, A. D., Leroy, A. K., Jameson, K., et al. 2011, [ApJ](#), **741**, 12
- Brunt, C. M., Heyer, M. H., & Mac Low, M. M. 2009, [A&A](#), **504**, 883
- Caselli, P., Benson, P. J., Myers, P. C., & Tafalla, M. 2002, [ApJ](#), **572**, 238
- Caselli, P., & Myers, P. C. 1995, [ApJ](#), **446**, 665
- Chen, H. H.-H., Offner, S. S. R., Pineda, J. E., et al. 2020, [arXiv e-prints](#), [arXiv:2006.07325](#)
- Chen, H. H.-H., Pineda, J. E., Goodman, A. A., et al. 2019, [ApJ](#), **877**, 93
- Chevance, M., Madden, S. C., Fischer, C., et al. 2020, [MNRAS](#), **494**, 5279
- Chevance, M., Kruijssen, J. M. D., Vazquez-Semadeni, E., et al. 2020, [SSRv](#), **216**, 50
- Clark, P. C., & Glover, S. C. O. 2015, [MNRAS](#), **452**, 2057
- de los Reyes, M. A. C., & Kennicutt, Robert C., J. 2019, [ApJ](#), **872**, 16
- Dessauges-Zavadsky, M., Richard, J., Combes, F., et al. 2019, [NatAs](#), **3**, 1115
- Dobbs, C. L. 2015, [MNRAS](#), **447**, 3390
- Field, G. B., Blackman, E. G., & Keto, E. R. 2011, [MNRAS](#), **416**, 710
- Fukui, Y., Kawamura, A., Minamidani, T., et al. 2008, [ApJS](#), **178**, 56

- Galametz, M., Madden, S., Galliano, F., et al. 2009, *A&A*, 508, 645
- Girichidis, P., Federrath, C., Banerjee, R., & Klessen, R. S. 2011, *MNRAS*, 413, 2741
- Glover, S. C. O., & Clark, P. C. 2012, *MNRAS*, 421, 9
- Glover, S. C. O., Federrath, C., Mac Low, M. M., & Klessen, R. S. 2010, *MNRAS*, 404, 2
- Glover, S. C. O., & Mac Low, M.-M. 2011, *MNRAS*, 412, 337
- Gong, M., Ostriker, E. C., & Kim, C.-G. 2018, *ApJ*, 858, 16
- Gong, M., Ostriker, E. C., Kim, C.-G., & Kim, J.-G. 2020, *ApJ*, 903, 142
- Goodman, A. A., Barranco, J. A., Wilner, D. J., & Heyer, M. H. 1998, *ApJ*, 504, 223
- Gordon, K. D., Meixner, M., Meade, M., et al. 2011, *AJ*, 142, 102
- Grenier, I. A., Casandjian, J.-M., & Terrier, R. 2005, *Sci*, 307, 1292
- Harris, C. R., Millman, K. J., van der Walt, S. J., et al. 2020, *Nature*, 585, 357
- Heyer, M., Krawczyk, C., Duval, J., & Jackson, J. M. 2009, *ApJ*, 699, 1092
- Heyer, M. H., & Brunt, C. M. 2004, *ApJL*, 615, L45
- Hughes, A., Wong, T., Ott, J., et al. 2010, *MNRAS*, 406, 2065
- Hughes, A., Meidt, S. E., Colombo, D., et al. 2013, *ApJ*, 779, 46
- Hunter, J. D. 2007, *Computing in Science & Engineering*, 9, 90
- Jameson, K. E., Bolatto, A. D., Leroy, A. K., et al. 2016, *ApJ*, 825, 12
- Jameson, K. E., Bolatto, A. D., Wolfire, M., et al. 2018, *ApJ*, 853, 111
- Juvela, M., Malinen, J., Montillaud, J., et al. 2018, *A&A*, 614, A83
- Kalari, V. M., Rubio, M., Saldaño, H. P., & Bolatto, A. D. 2020, *MNRAS*, 499, 2534
- Kauffmann, J., Pillai, T., & Goldsmith, P. F. 2013, *ApJ*, 779, 185
- Kennicutt, Robert C., J., Calzetti, D., Walter, F., et al. 2007, *ApJ*, 671, 333
- Kim, S., Rosolowsky, E., Lee, Y., et al. 2007, *ApJS*, 171, 419
- Krumholz, M. R. 2012, *ApJ*, 759, 9
- Langer, W. D., Velusamy, T., Pineda, J. L., Willacy, K., & Goldsmith, P. F. 2014, *A&A*, 561, A122
- Larson, R. B. 1981, *MNRAS*, 194, 809
- Lee, E. J., Chang, P., & Murray, N. 2015, *ApJ*, 800, 49
- Lee, M.-Y., Stanimirović, S., Douglas, K. A., et al. 2012, *ApJ*, 748, 75
- Leroy, A. K., Walter, F., Brinks, E., et al. 2008, *AJ*, 136, 2782
- Leroy, A. K., Bolatto, A., Bot, C., et al. 2009, *ApJ*, 702, 352
- Leroy, A. K., Schinnerer, E., Hughes, A., et al. 2021, *ApJS*, 257, 43
- Li, Q., Narayanan, D., Davè, R., & Krumholz, M. R. 2018, *ApJ*, 869, 73
- Lin, Y., Wyrowski, F., Liu, H. B., et al. 2021, *arXiv e-prints*, arXiv:2112.01115
- MacLaren, I., Richardson, K. M., & Wolfendale, A. W. 1988, *ApJ*, 333, 821
- Madden, S. C., Galliano, F., Jones, A. P., & Sauvage, M. 2006, *A&A*, 446, 877
- Madden, S. C., Cormier, D., Hony, S., et al. 2020, *A&A*, 643, A141
- Muraoka, K., Homma, A., Onishi, T., et al. 2017, *ApJ*, 844, 98
- Ochsendorf, B. B., Meixner, M., Roman-Duval, J., Rahman, M., & Evans, N. J. 2017, *ApJ*, 841, 109
- Oka, T., Hasegawa, T., Sato, F., et al. 2001, *ApJ*, 562, 348
- Palmeirim, P., André, P., Kirk, J., et al. 2013, *A&A*, 550, A38
- Paradis, D., Dobashi, K., Shimoikura, T., et al. 2012, *A&A*, 543, A103
- Parmentier, G. 2020, *ApJ*, 893, 32
- Parmentier, G., & Pasquali, A. 2020, *ApJ*, 903, 56
- Passot, T., Pouquet, A., & Woodward, P. 1988, *A&A*, 197, 228
- Pattle, K. 2016, *MNRAS*, 459, 2651
- Pineda, J. E., Goodman, A. A., Arce, H. G., et al. 2010, *ApJL*, 712, L116
- Pineda, J. L., Langer, W. D., Velusamy, T., & Goldsmith, P. F. 2013, *A&A*, 554, A103
- Pirogov, L. E. 2009, *ARep*, 53, 1127
- Planck Collaboration, Ade, P. A. R., Aghanim, N., et al. 2011, *A&A*, 536, A19
- Plummer, H. C. 1911, *MNRAS*, 71, 460
- Ridge, N. A., Francesco, J. D., Kirk, H., et al. 2006, *AJ*, 131, 2921
- Rubele, S., Girardi, L., Kerber, L., et al. 2015, *MNRAS*, 449, 639
- Rubio, M., Elmegreen, B. G., Hunter, D. A., et al. 2015, *Nature*, 525, 218
- Saldaño, H. P., Rubio, M., Jameson, K., & Bolatto, A. D. 2018, *BAAA*, 60, 192
- Schneider, N., André, P., Könyves, V., et al. 2013, *ApJL*, 766, L17
- Schruba, A., Kruijssen, J. M. D., & Leroy, A. K. 2019, *ApJ*, 883, 2

- Schruba, A., Leroy, A. K., Walter, F., et al. 2012, *AJ*, **143**, 138
- Schruba, A., Leroy, A. K., Kruijssen, J. M. D., et al. 2017, *ApJ*, **835**, 278
- Shetty, R., Beaumont, C. N., Burton, M. G., Kelly, B. C., & Klessen, R. S. 2012, *MNRAS*, **425**, 720
- Shetty, R., Glover, S. C., Dullemond, C. P., & Klessen, R. S. 2011a, *MNRAS*, **412**, 1686
- Shetty, R., Glover, S. C., Dullemond, C. P., et al. 2011b, *MNRAS*, **415**, 3253
- Smith, R. J., Glover, S. C. O., Clark, P. C., Klessen, R. S., & Springel, V. 2014, *MNRAS*, **441**, 1628
- Solomon, P. M., Rivolo, A. R., Barrett, J., & Yahil, A. 1987, *ApJ*, **319**, 730
- Sun, J., Leroy, A. K., Schruba, A., et al. 2018, *ApJ*, **860**, 172
- Sun, J., Leroy, A. K., Ostriker, E. C., et al. 2020, *ApJ*, **892**, 148
- Szűcs, L., Glover, S. C. O., & Klessen, R. S. 2016, *MNRAS*, **460**, 82
- Tang, M., Liu, T., Qin, S.-L., et al. 2018, *ApJ*, **856**, 141
- Tatematsu, K., Umemoto, T., Kandori, R., & Sekimoto, Y. 2004, *ApJ*, **606**, 333
- Traficante, A., Duarte-Cabral, A., Elia, D., et al. 2018, *MNRAS*, **477**, 2220
- Valdivia-Mena, M. T., Rubio, M., Bolatto, A. D., Saldaño, H. P., & Verdugo, C. 2020, *A&A*, **641**, A97
- Vázquez-Semadeni, E., Palau, A., Ballesteros-Paredes, J., Gómez, G. C., & Zamora-Avilés, M. 2019, *MNRAS*, **490**, 3061
- Velusamy, T., Langer, W. D., Pineda, J. L., et al. 2010, *A&A*, **521**, L18
- Volgenau, N. H., Mundy, L. G., Looney, L. W., & Welch, W. J. 2006, *ApJ*, **651**, 301
- Whitworth, A. P., & Ward-Thompson, D. 2001, *ApJ*, **547**, 317
- Wolfire, M. G., Hollenbach, D., & McKee, C. F. 2010, *ApJ*, **716**, 1191
- Wong, T., Hughes, A., Fukui, Y., et al. 2009, *ApJ*, **696**, 370
- Wong, T., Hughes, A., Tokuda, K., et al. 2019, *ApJ*, **885**, 50
- Xu, D., Li, D., Yue, N., & Goldsmith, P. F. 2016, *ApJ*, **819**, 22
- Zucker, C., Goodman, A., Alves, J., et al. 2021, *ApJ*, **919**, 35